

Sol-gel Barium Titanate Nanohole Array as a Nonlinear Metasurface and a Photonic Crystal

Ülle-Linda Talts*[1], Helena C. Weigand[1], Grégoire Saerens[1], Peter Benedek[2], Joel Winiger[3], Vanessa Wood[2], Jürg Leuthold[3], Viola Vogler-Neuling[1,4], Rachel Grange[1]

[1] Optical Nanomaterial Group, Institute for Quantum Electronics, Department of Physics, ETH Zurich, HPT H10, Auguste-Piccard-Hof 1, 8093 Zurich, Switzerland

Email Address: utalts@phys.ethz.ch

[2] Institute for Electromagnetic Fields, Department of Information Technology and Electrical Engineering, ETH Zurich, ETZ H96, Gloriastrasse 35, 8092 Zurich, Switzerland

[3] Institute for Electronics, Department of Information Technology and Electrical Engineering, ETH Zurich, ETZ H96, Gloriastrasse 35, 8092 Zurich, Switzerland

[4] Soft Matter Physics Group, Adolphe Merkle Institute, University of Fribourg, Chemin des Verdiers 4, Fribourg, 1700, Switzerland

The quest of a nonlinear optical material that can be easily nanostructured over a large surface area is still ongoing. Here, we demonstrate a nanoimprinted nonlinear barium titanate 2D nanohole array that shows optical properties of a 2D photonic crystal and metasurface, depending on the direction of the optical axis. The challenge of nanostructuring the inert metal-oxide is resolved by direct soft nanoimprint lithography with sol-gel derived barium titanate enabling critical dimensions of 120 nm with aspect ratios of 5. The nanohole array exhibits a photonic bandgap in the infrared range when probed along the slab axis while lattice resonant states are observed in out-of-plane transmission configuration. The enhanced light-matter interaction from the resonant structure enables to increase the second-harmonic generation in the near-UV by a factor of 18 illustrating the potential in the flexible fabrication technique for barium titanate photonic devices.

1 Introduction

Nonlinear optics has greatly expanded the field of photonics with phenomena such as frequency conversion processes and quantum light generation. While current applications of these photon-photon interactions rely primarily on high-intensity optical sources and bulky crystals, new strategies are being developed to enhance the intrinsically weak higher-order nonlinear effects. Combining nanostructures with a nonlinear optical medium has demonstrated to increase the efficiency of parametric quantum processes such as second harmonic generation (SHG) [1], sum-frequency generation [2], four-wave mixing [3] or spontaneous parametric down-conversion [4].

Several material platforms support these nonlinear processes yet certain drawbacks have limited their applicability. III-V materials have strong nonlinear coefficients but signals can

be screened by the substrate required for epitaxial growth or the second-order nonlinear optical susceptibility tensor is oriented unfavorably for out-of-plane excitation [5, 6]. Poled polymers show an impressive modulation efficiency with an order of magnitude larger electro-optic coefficient compared to lithium niobate, but the material stability is hindering its use in long-term applications [7, 8]. Plasmonic structures permit the highest electric field confinement but they are subject to high optical losses and low damage threshold [9].

Non-centrosymmetric metal-oxides, firstly only available as bulk crystals, show rather large second-order susceptibility coefficients, high damage threshold and a wide transparency range. These properties are exploited for optical modulators and laser gain media [10]. The recent advances in fabrication of lithium niobate on insulator devices have demonstrated the potential in combining these metal-oxide thin films with advanced nanofabrication for miniaturized and efficient optical devices such as high-speed electro-optic modulators and on-chip optical parametric oscillators, to name a few [11]. Also other metal-oxides such as barium titanate [10], barium borate [12], potassium niobate [13] and potassium titanyl phosphate [14] have the potential to be an alternative nonlinear optical material platform. However, the limited thin film availability and the transferability of CMOS nanofabrication processes make it challenging, motivating the search for novel nanofabrication approaches.

We choose to focus on barium titanate (BaTiO_3 , or BTO), a metal-oxide with intrinsic nonlinear optical processes, characterized by a second-order susceptibility tensor of $d_{15}=15.7 \text{ pmV}^{-1}$ in thin film, energy gap of 3.5 eV (low optical material losses above 354 nm), ultra-high electro-optic response of $r_{15}=1300 \text{ pmV}^{-1}$ in the unclamped case and physical resilience to mechanical as well as optical damage [10]. Due to the chemical inertness, insulating nature and no commercial availability of high quality thin film wafers, nanofabrication of the metal-oxide photonic crystals (PhC) and metasurfaces has been challenging using a similar nanolithography approach as for semiconductor devices [15, 16]. Molecular beam epitaxy deposited BTO thin films have been used for active photonic integrated circuits. Due to the limited thickness of the achieved films and challenging etching, hybrid structures with other semiconductors are needed to form light guiding films [16, 17].

In a previous publication, we have reported BTO metasurfaces with 15 times increased SHG in the near-UV range by a hybrid device with a SiN_x capping layer to form the resonant nanodisk arrays [1]. To achieve both previously mentioned structures, focused ion beam milling or electron-beam lithography with plasma etching was employed, requiring highly specialized and optimized tools. Here we report on an alternative fabrication technique to circumvent the need for hybrid structures as well as the difficulty to pattern and etch the chemically resistant and insulating metal-oxide.

Bottom-up fabrication via direct soft nanoimprint lithography (SNIL) has the precision of top-down fabrication and the flexibility to be applied to novel materials without developing

a new etching recipe [18]. Most commonly this technique uses polydimethylsiloxane (PDMS) stamps, fabricated as an inverse from a nanostructured Si-based master mold. This enables imprinting the desired structures into the material of interest. It is an established method for patterning photoresists for top-down fabrication, but directly imprinting nanoparticles and sol-gel solutions has been shown as another route for highly-scalable nanopatterning of metal-oxides [18].

Nanoparticles of BTO above 30 nm have similar crystal properties as the bulk crystal [19] and since they can be dispersed in a solvent, molding the particles into periodic structures is possible [20]. However, due to the limited packing density and inherent rough surfaces of nanoparticle assemblies, achieving resonant photonic structures has been difficult due to scattering. An alternative to nanoparticle solutions are sol-gels, which form a polymer-like metal-oxide network in a solution and becomes a dense xerogel thin film after annealing [21]. Lithium niobate nanohole arrays have been made by capillary imprinting an aqueous sol-gel and the authors observed SHG enhancement when combined with gold particles [22]. Effective electric field confinement in nanoimprinted polycrystalline PhC has shown to enable quasi-CW lasing in metal halide perovskite, but similar increased light-matter interaction has not been shown in bottom-up fabricated nonlinear metal-oxide structures [23].

Sol-gel derived BTO 2D PhC formed a photonic bandgap[24] and while the investigation of this metal-oxide's electro-optic properties established a competitive value with thin film lithium niobate [21], the optical nonlinear properties are still largely unexplored.

Because high quality PhC underly devices such as high Purcell factor cavity resonators [25, 26, 27], dispersionless and low loss waveguides [28] or topological insulators [29], we choose a design of a hexagonal nanohole array in solution-processed BTO slab. Air holes resonant at specific wavelengths have also been realized for low-loss Mie-resonant cavities [30] and sensors with high energy confinement at metasurface-air interface [31]. Similarly, nanohole arrays in a nonlinear optical material slab, such as BTO, increase the light-matter interaction and SHG [1, 26, 27]. Using direct SNIL to pattern the sol-gel BTO, we achieve high aspect ratios of 5 and minimized scattering from the smooth side-walls. The in-plane and out-of-plane light interaction in the bottom-up fabricated structures is characterized by measuring a slab photonic crystal bandgap and Mie surface lattice resonances, respectively. Additionally, we show that the sol-gel derived films have nonlinear optical properties which can be enhanced by the nanostructures indicating this technique can be used to increase the nonlinear light generation or electro-optic modulation efficiency.

2 Results and Discussion

2.1 Barium Titanate Sol-gel and Nanoimprinting

For the SNIL process depicted in **Figure 1a**, a BTO sol-gel solution was prepared following a previously reported recipe for electro-optically active solution-derived BTO [21].

The solution was produced in ambient conditions, without a specialized glove-box and thus allows scaled-up fabrication by e.g. a roll-to-roll process [32]. In order to confirm the properties of the resulting material and estimate the effective refractive index for designing the nanohole arrays, a 650 nm thick characterization film was prepared alongside with the imprinted structures. X-ray diffraction measurements on the thin films confirmed the characteristic features of tetragonal and orthorhombic crystalline phases after annealing at 800 °C (Figure S1a, Supporting Information). Prism coupling measurements show an effective refractive index value of 1.87 for 983 nm source (Figure S1b, Supporting Information) which is higher than has been previously reported in nanoparticle films confirming the reduced porosity [10]. Based on the measured refractive index, we design a hexagonal nanohole array with a periodicity of 612 nm, for an estimated dielectric bandgap edge at 1500 nm, to be imprinted into the liquid state sol-gel BTO. Transparent fused quartz was used as a substrate to enable linear and nonlinear characterization in transmission configuration. SEM images of the annealed structures retained the designed periodicity while shrinkage was observed (Figure 1c *xy*-plane and 1d *xz*-plane) as has been reported previously for direct imprinting into sol-gel [18]. We observe smooth side-wall surface and a uniform material filling in the mold from the imaged cross-section in Figure 1d. By optimizing the spin-coating parameters, the residual film could be reduced to only 20 nm. The approximately 15° tilt in the structures result from the slight shift when placing the mold manually on the spin-coated sol-gel solution. We achieved an aspect ratio close to 5 (570 nm/120 nm) with critical dimensions as small as 120 nm (SI. Figure S2). The nanohole arrays used for further optical characterization have a period of 612 nm, radius of 210 nm and thickness of 570 nm.

2.2 Reflection and Transmission in the Photonic Crystal and Metasurface Configuration

The evaluation of the slab reflection and transmission spectra of the nanohole array enables to illustrate the interesting duality of PhC and metasurface behaviour, where a periodic structure supports several discrete resonance modes[33]. We use a supercontinuum white light laser and a spectrometer to experimentally show these eigenmodes at different illumination configurations (details included in the Experimental Section and Supporting Information). First, we simulate and observe a PhC optical bandgap by measuring the reflection spectrum for in-plane light propagation (illumination configuration in **Figure 2a**, setup schematic in

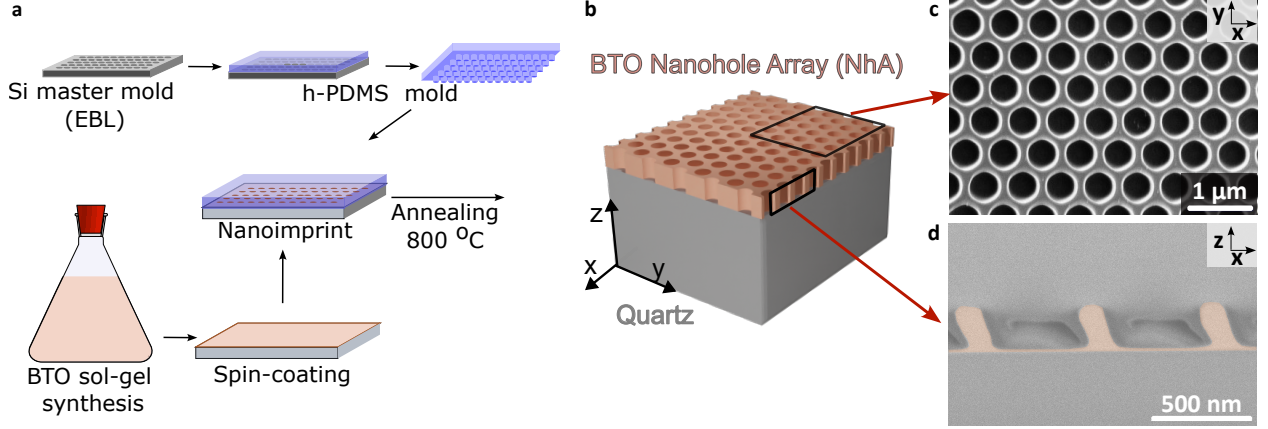


Figure 1: (a) Process flow of the direct soft nanoimprint lithography (SNIL) used for transferring the pattern from a Si master mold made with electron-beam lithography to sol-gel BTO. (b) Schematic of the resulting nanohole array in a BTO slab on a fused quartz substrate. (c) Scanning electron microscopy (SEM) image of a chromium coated BTO nanohole array in xy -plane. (d) SEM image of the nanohole array cross-section cut in xz -plane made with focused ion beam milling. BTO structures are shaded orange. The dark grey features between the structures are from ion beam deposition used for imaging.

Figure S3, Supporting Information) from a sample cleaved along the x -axis (along Γ -M reciprocal axis). We implemented the 2D plane wave expansion method [34] with the geometrical parameters obtained from SEM images to estimate the energy band structure (Figure 2b). Our measurements show a strong reflection band with transverse electric (TE) polarization in the calculated wavelength range corresponding to the bandgap (Figure 2b, 2c), bandgap highlighted in orange). No bandgap was expected for the transverse magnetic (TM) polarization guided in the film and, indeed, a significantly suppressed reflection (Figure 2b, 2c) was detected.

The oscillation in the reflection can be attributed to the Fabry-Pérot resonances formed between the different imprinted nanohole array sets in the BTO slab which have a distance of 25 μm (Figure S3, Supporting Information). These reflection measurements coincide well with the simulations and show a strong TE bandgap in the IR range. The ability to fabricate PhC with optimized bandgap range is important for further research into more complex devices such as BTO PhC waveguides and high Purcell factor dielectric resonators in the VIS range.

To characterize the nanohole array metasurface properties, an equivalent structure was probed perpendicularly to the 2D array to excite coupled Mie resonances within the air holes or in the BTO slab (**Figure 3a**).

Finite-difference time-domain (FDTD) simulations show two distinct resonances (Figure 3 b): at 774 nm and at 786 nm. The model was built based on parameters inferred from the SEM images and estimate of the refractive index: a period of 612 nm, a radius of 210 nm, a height of 570 nm, a constant refractive index of 1.97 between 700 and 900 nm. As the cross-section images show (Figure 1d), the packing density in the structures is high

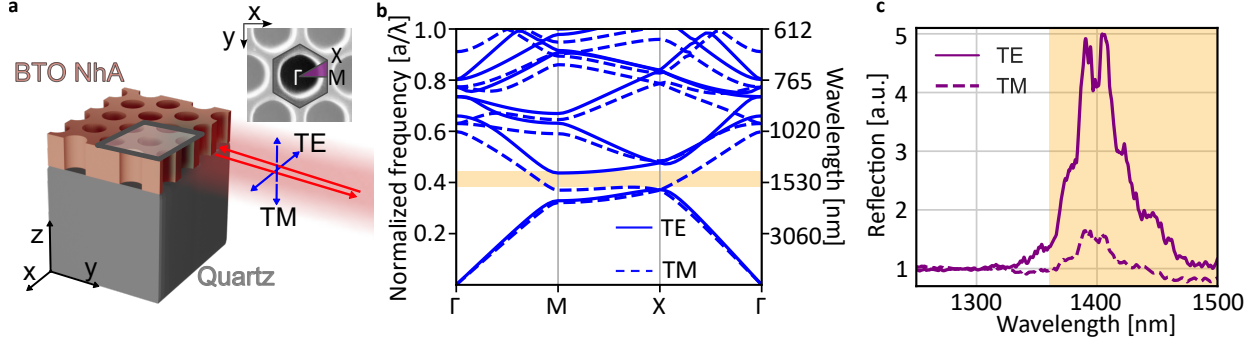


Figure 2: (a) Reflection measurement configuration with the first Brillouin zone shaded grey in the inset. Electric field polarization vector is shown for the TE and TM coupling modes. (b) Calculated energy band diagram for the structures in Figure 1 with the TE photonic bandgap highlighted yellow. (c) Measured reflection spectra of the slab PhC in M – X light propagation direction with the highlighted yellow region corresponding to (b). Both TE and TM reflection spectra are normalized to measurements from an unstructured area.

thus an increased effective refractive index compared to the thin films is expected. The transmission spectra match well with the simulation results and only a slight red shift was observed experimentally with detected resonances at 782 nm and 797 nm (Figure 3c). The strongest extinction measured at 782 nm has a quality factor of 78. This is lower than the state-of-the-art nonlinear metal-oxide resonators with 3 orders of magnitude higher quality factor values shown in lithium niobate [35] but further design optimization and methods to achieve free-standing or embedded structures for symmetric field distribution are expected to considerably improve these parameters. We also confirm the poly-crystalline nature of the nanostructured BTO by a polarization independent extinction at resonance in simulations as well as in the measured spectra (Figure 3b and 3c, respectively).

Analysis of the simulated electric and magnetic field profiles (Figure S4, Supporting Information) within the metasurface at the two resonances enables us to determine the different excited modes (the xz -plane cross-section schematic annotated in Figure 3d). At higher energy resonances (Figure 3e), 774 nm in FDTD simulation and 782 nm in measurements, the electric field is strongly confined into the air holes with field lines along the polarization direction resembling a coupled electric dipole in a surface lattice resonant mode (ED-SLR) [31, 36]. At higher wavelength resonances Figure 3f, 786 nm in FDTD simulation and 797 nm in measurements, strong circulating electric fields with minima in the middle are characteristic to collective coupling of a magnetic dipole and thus can be attributed to magnetic dipole surface lattice resonant mode (MD-SLR) (Figure S4f, Supporting Information) [36]. The strongest electric field enhancement in the nanohole array is observed at the ED-SLR with up to 14 Vm^{-1} field in air holes and a mean average field enhancement by 5 in the BTO structures compared to same thickness thin film (Figure 3e). More advanced designs are expected to increase or optimize the local field confinement even further and can be adapted

depending on the desired application [30, 31, 34].

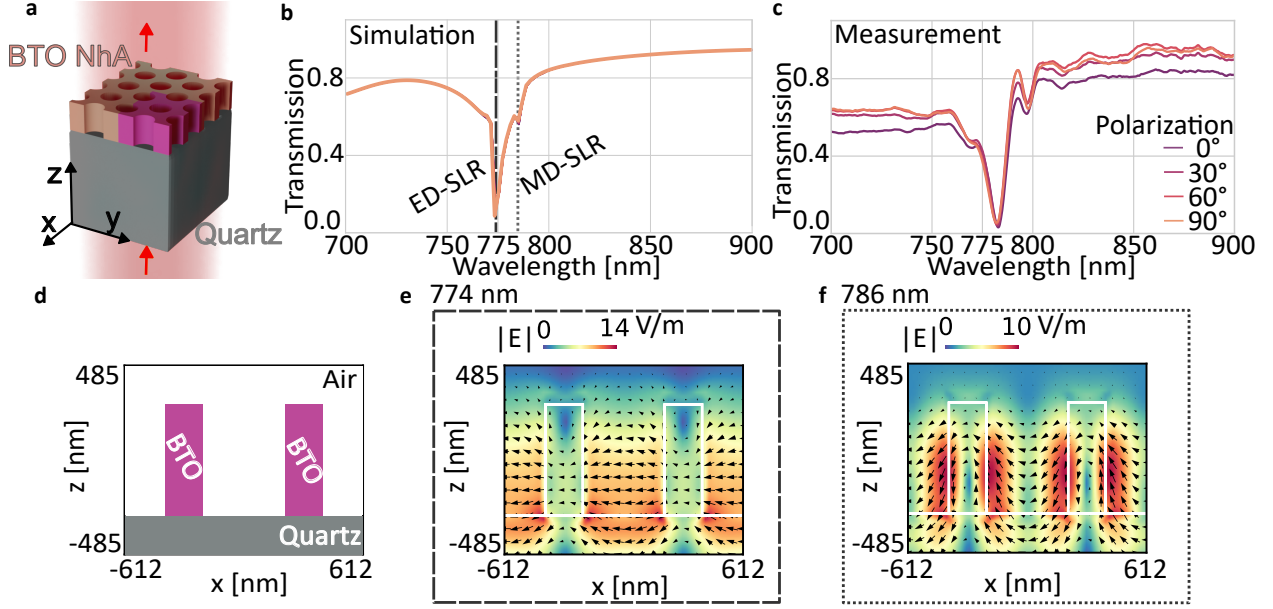


Figure 3: (a) Schematic of the hexagonal nanohole array with excitation along the z -axis direction. The red shading represents the probing laser. The unit cell used for further analysis of the fields is indicated with the purple highlighted area. Polarization independent transmission analysis: (b) simulated transmission spectra with an overlay of 0° to 90° polarization, (c) measured polarization independent transmission of the nanohole array. (d) Schematic of the material distribution in the xz -plane cross-section used in part (e) and (f). (e) Simulated absolute electric field at 774 nm in the xz -plane. (f) Simulated absolute electric field at 786 nm in the xz -plane. Arrows represent the real part of the electric field in the xz -plane. The cross-sections are taken from the middle of the unit cell in the xz -plane. The plane wave source polarization is kept parallel to the x -axis.

2.3 Nonlinear signal enhancement in metasurface

Taking advantage of the large transparency window and the nanohole array enabled field enhancement, we investigate here the SHG of solution derived BTO in the near-UV (375-425 nm). Additionally to XRD measurements (SI Figure S1), the formation of the tetragonal crystal phase was further confirmed by the spectral characterization of SHG. The BTO film and nanohole array were probed in the transmission configuration as illustrated in **Figure 4** a with a Ti-sapphire laser (140 fs, FWHM 10 nm, setup details in the Experimental Section). The spectrum of the SHG in the sol-gel thin film and the PhC at 780 nm excitation (at the ED-SLR as in Figure 3b) is shown in Figure 4b. A further evaluation of the SHG in sol-gel BTO films and imprinted structures confirmed the expected quadratic power dependence in the sol-gel derived BTO film and the nanohole array (Figure 4c). We observed that a poly-crystalline material without a preferred SHG orientation is achieved for all fundamental laser excitation polarizations along the thin film plane (Figure 4d, grey marker). In this poly-crystalline sample, the overlap of dipolar and quadrupolar polarization dependent SHG

intensity plots is effectively averaged to an isotropic SHG when different orientations of the crystals are probed simultaneously. A similar homogeneous polarization independent SHG intensity was observed in the PhC at an arbitrary wavelength (Figure 4d, blue marker) while polarization dependent SHG was observed at the resonance (Figure 4d, purple marker). Simulations show that a polarization along the y -axis forms a ED-SLR with a weaker dipole also inside the BTO slab resulting in increased maximum electric field (Figure S4c, Supporting Information), which explains the polarization dependence of the SHG at this resonance. A wavelength dependent SHG intensity was observed only in the nanohole array structures with an 18 times increased conversion efficiency at the ED-SLR and a 10 times increase at the MD-SLR (Figure 4e and 4f). The SHG shows a similar enhancement magnitude as is expected from the electric field confinement in Figure 3e and 4f. Our results show that the proposed method of combining the sol-gel derived BTO and nanostructures allows to considerably increase the SHG efficiency.

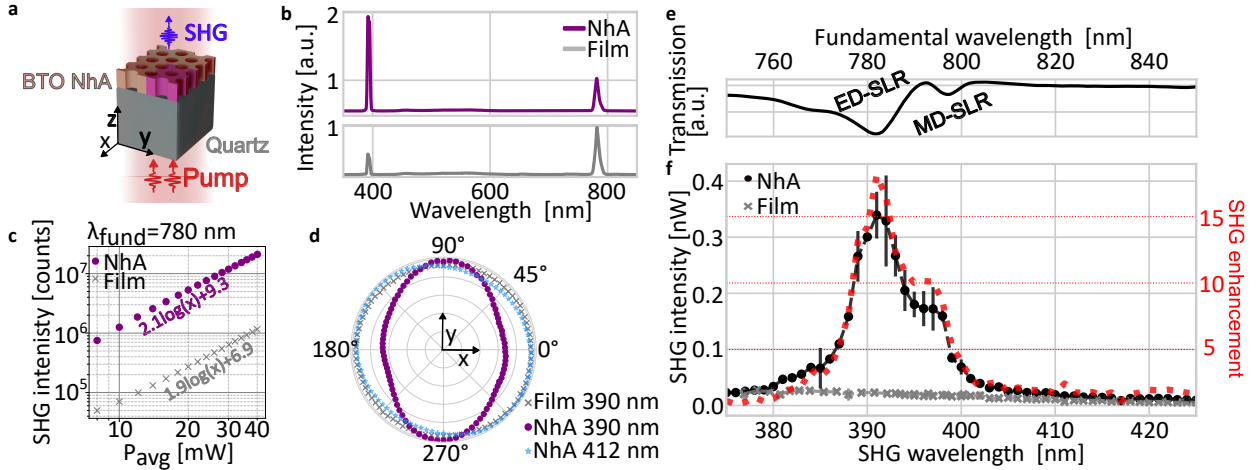


Figure 4: (a) Schematic of the SHG characterization setup. (b) Measured SHG spectra with fundamental laser at 780 nm reduced by a band pass filter (10^{-5} reduction at pump). (c) SHG intensity dependence on the excitation power for the nanohole array and film at 780 nm excitation. (d) Polarization dependent SHG intensity for the sol-gel thin film at 390 nm, the nanohole array at 390 nm and off-resonance (412 nm) emission. All measurements are normalized to the maximum of each measurement set. (e) Linear transmission spectrum from Figure 3(c) rescaled for comparison. (f) Pump wavelength dependent SHG emission for the film (grey markers) and the nanohole array (black markers) at an average laser power of the fundamental pump at 50 mW. The SHG enhancement by the nanostructures ($P_{\text{NhA}}/P_{\text{Film}}$) is plotted in the same graph in red. Deviations are determined from 3 separately aligned measurements.

3 Conclusion

In summary, we introduce a highly scalable method of combining sol-gel chemistry and soft nanoimprint lithography to produce nonlinear metal-oxide nanohole arrays. In addition to previously reported electro-optic properties [21], we show that the sol-gel derived BTO

exhibits second-order optical nonlinearity. The sol-gel forms an isotropic poly-crystalline material without preferred grain orientation which averages the overall effective $\chi^{(2)}$ tensor. Nevertheless, the random grain orientation has been shown to be beneficial for random quasi phase-matching where the SHG scales linearly with the propagation volume [37]. The resulting independence from coherence length makes sol-gel BTO, and other solution processed non-centrosymmetric metal-oxides, an easily scalable material platform for broadband frequency conversion optical components.

Additionally, we show that solution-based processing enables to produce high aspect ratio and smooth side-wall nanostructures that exhibit PhC as well as metasurface characteristics, depending on light propagation direction. This duality in optical properties enables to design multifunctional optical devices that can control routing in-plane via e.g. photonic crystal waveguides [26] and meanwhile also locally couple in external radiation by behaving as nanoantennas [30]. We have experimentally shown the theoretically predicted enhancement in electric field confinement by over 18 times increased SHG efficiency at the resonance. Combining out-of-plane illumination induced coupled resonances with controlled slow light propagation in nonlinear material slab can potentially improve the frequency conversion efficiency further. Moreover, the large transparency window of BTO and the freedom to structure it on transparent insulating substrates enables to utilize the NUV and VIS spectrum range with minimized damage from absorption at high optical powers. The increased field in the electro-optic medium or in the nanohole cavities can be particularly beneficial for high-speed beam steering metasurfaces [38] or advanced nanohole array sensors [31]. This high-throughput fabrication platform is advantageous for improving the fabrication flexibility required for application optimized nonlinear photonic devices.

4 Experimental Section

Barium Titanate Sol-gel Synthesis:

Solution processed BTO sol-gel precursor was made following the procedure described by *Edmunson et. al.* [21]. Details of the exact chemicals applied in the synthesis are listed in the Supporting Information. 0.511 g of barium acetate is diluted in 10 ml of glacial acetic acid by stirring for an hour. 5 °C water bath is prepared for combining 426 μ l of acetylacetate with 592 μ l titanium isopropoxide. Barium acetate solution in acetic acid is added to make a 1:1 stoichiometric ratio of Ba:Ti in a 0.2 M solution of the metal cations. The solution is stirred for 24 h before 1:1 volume ratio dilution in anhydrous methanol to make a 0.1 M solution that is used for imprinting.

Hybrid-PDMS Mold Preparation and Direct Imprinting:

The master mold for SNIL was prepared using electron beam lithography and dry reactive

ion etching process. For the hybrid PDMS mold, hard-PDMS (hPDMS, Gelest Inc.) was first spin-coated on the Si master mold followed by embedding the whole mold in soft-PDMS (SylgardTM 184 Elastomer Kit) to form a 2-4 mm thick mold. The hybrid PDMS was cured at 65 °C for 72 hours before separating from the master mold. Mold preparation details are included in Supporting Information. 20 μ l of BTO sol-gel dilution was spin-coated (950 rpm, 1000 rpm/s, 5 sec) on plasma treated fused quartz substrate with the hybrid PDMS mold placed on top directly after. The mold with a 5 g weight placed on top was left to cure at 60 °C for 15 hours before removal. The chip was annealed in ambient atmosphere to 800 °C with heating and cooling rate of 2 °Cmin⁻¹.

Slab Reflection Measurement:

Slab reflection measurements were done in a custom microscopy setup for probing a cleaved sample with structured areas close to the cleaved edge. Broadband IR light was focused and collected from the sample edge with 20x objective (NA=0.22, Zeiss) and the output light was coupled to a spectrometer. Focal point of the excited area was confirmed with an additional camera visualizing the sample top-down perpendicularly to the surface and beam path. Details of the setup and can be found in Figure S3, Supporting Information.

Transmission Characterization:

Transmission measurements were done in a collinear microscopy setup with light focused on the nanohole array with a lens (LA1131 f=50mm , Thorlabs), collected from the crystal area by a 100x objective (NA=0.75, Zeiss) and the output light was coupled to a spectrometer (Andor Schamrock, Andor Newton CCD) via a reflective collimator and a multimode fiber.

Simulations:

The nanohole array design was optimized using FDTD simulations (Ansys Lumerical) and the design was iterated to account for fabrication changes due to structure transfer using the PDMS mold and sol-gel shrinkage during solvent evaporation. Periodic Bloch boundaries were used in the x - and y -plane while perfectly matched layer boundary condition was used for both extremes of the z -plane. Field monitors were placed in the middle of the slab in xy -plane and through the middle of the nanoholes in xz -plane. Electric field and magnetic field absolute and vector plots at the resonances are included in the Figure S4, Supporting Information.

Second Harmonic Generation Characterization:

SHG was characterized in transmission using a custom built microscopy set-up with a Ti:Sapphire laser source where the laser was focused on the sample with a lens (LA1131 f=50 mm, Thorlabs) and signal was collected with a 100x objective (NA=0.8, Olympus). The signal was captured in a sCMOS camera (Andor Zyla sCMOS) equipped with two short-pass filters (FBG39, Thorlabs) for measuring the second harmonic output (one filter

for spectrum characterization). Setup and signal processing details are described in published work [1, 39] and included in the Supporting Information.

Supporting Information Supporting Information is available from the author. **Funding sources** This work was supported by the Swiss National Science Foundation Grant 179099 and 150609, the European Union’s Horizon 2020 research and innovation program from the European Research Council under the Grant Agreement No. 714837 (Chi2-nano-oxides) and No. 862346 (PolarNon). H.W. and U.T. acknowledge financial support from the Physics Department at ETH Zurich.

Acknowledgements

The authors acknowledge ScopeM and D-MATL X-Ray Service Platform at ETH Zurich for providing instrumentation for characterization, nanofabrication support from the operation team of the Binning and Rohrer Nanotechnology Center (BRNC) and the operation team of FIRST—Center for Micro and Nanoscience at ETHZ.

References

- [1] Flavia Timpu, Marc Reig Escalé, Maria Timofeeva, Nives Strkalj, Morgan Trassin, Manfred Fiebig, and Rachel Grange. Enhanced Nonlinear Yield from Barium Titanate Metasurface Down to the Near Ultraviolet. *Advanced Optical Materials*, 7(22):1900936, nov 2019.
- [2] Rocio Camacho-Morales, Lei Xu, Haizhong Zhang, Son Tung Ha, Leonid Krivitsky, Arseniy I. Kuznetsov, Mohsen Rahmani, and Dragomir Neshev. Sum-frequency generation in high-q gap metasurfaces driven by leaky-wave guided modes. *Nano Letters*, 22(15):6141–6148, 2022. PMID: 35867018.
- [3] Boyuan Jin and Christos Argyropoulos. Enhanced four-wave mixing with nonlinear plasmonic metasurfaces. *Scientific Reports*, 6(1), June 2016.
- [4] Tomás Santiago-Cruz, Anna Fedotova, Vitaliy Sultanov, Maximilian A. Weissflog, Dennis Arslan, Mohammadreza Younesi, Thomas Pertsch, Isabelle Staude, Frank Setzpfandt, and Maria Chekhova. Photon pairs from resonant metasurfaces. *Nano Letters*, 21(10):4423–4429, May 2021.
- [5] Sadao Adachi. Properties of Semiconductor Alloys: Group-IV, III-V and II-VI Semiconductors. *Prop. Semicond. Alloy. Group-IV, III-V II-VI Semicond.*, pages 1–400, mar 2009.
- [6] Sruti Menon and Varun Raghunathan. Polarization engineered second harmonic generation enhancement from amorphous silicon - gallium nitride heterogeneous resonant metasurface. *IEEE Journal of Selected Topics in Quantum Electronics*, 29(1: Nonlinear Integrated Photonics):1–8, 2023.
- [7] Fateh Ullah, Niping Deng, and Feng Qiu. Recent progress in electro-optic polymer for ultra-fast communication. *Photonix*, 2(1):1–18, dec 2021.

- [8] Iman Taghavi, Maryam Moridsadat, Alexander Tofini, Shaheer Raza, Nicolas A. F. Jaeger, Lukas Chrostowski, Bhavin J. Shastri, and Sudip Shekhar. Polymer modulators in silicon photonics: review and projections. *Nanophotonics*, 11(17):3855–3871, 2022.
- [9] Robert W. Boyd. *Nonlinear Optics*. Elsevier Inc., 2008.
- [10] Artemios Karvounis, Flavia Timpu, Viola V. Vogler-Neuling, Romolo Savo, and Rachel Grange. Barium Titanate Nanostructures and Thin Films for Photonics. *Advanced Optical Materials*, 8(24), dec 2020.
- [11] Andreas Boes, Lin Chang, Carsten Langrock, Mengjie Yu, Mian Zhang, Qiang Lin, Marko Lončar, Martin Fejer, John Bowers, and Arnan Mitchell. Lithium niobate photonics: Unlocking the electromagnetic spectrum. *Science*, 379(6627):eabj4396, 2023.
- [12] Alexander S. Solntsev, Girish S. Agarwal, and Yuri S. Kivshar. Metasurfaces for quantum photonics. *Nature Photonics*, 15(5):327–336, April 2021.
- [13] Christof Dues, Marius J. Müller, Sangam Chatterjee, Claudio Attaccalite, and Simone Sanna. Nonlinear optical response of ferroelectric oxides: First-principles calculations within the time and frequency domains. *Phys. Rev. Mater.*, 6:065202, Jun 2022.
- [14] Cristine Calil Kores, Carlota Canalias, and Fredrik Laurell. Quasi-phase matching waveguides on lithium niobate and KTP for nonlinear frequency conversion: A comparison. *APL Photonics*, 6(9), 09 2021. 091102.
- [15] Helena Weigand, Viola V. Vogler-Neuling, Marc Reig Escalé, David Pohl, Felix U. Richter, Artemios Karvounis, Flavia Timpu, and Rachel Grange. Enhanced electro-optic modulation in resonant metasurfaces of lithium niobate. *ACS Photonics*, 8(10):3004–3009, 2021.
- [16] Peter Girouard, Pice Chen, Young Kyu Jeong, Zhifu Liu, Seng-Tiong Ho, and Bruce W. Wessels. $\chi^{(2)}$ modulator with 40-ghz modulation utilizing batio3 photonic crystal waveguides. *IEEE Journal of Quantum Electronics*, 53(4):1–10, 2017.
- [17] Felix Eltes, Gerardo E. Villarreal-Garcia, Daniele Caimi, Heinz Siegwart, Antonio A. Gentile, Andy Hart, Pascal Stark, Graham D. Marshall, Mark G. Thompson, Jorge Barreto, Jean Fompeyrine, and Stefan Abel. An integrated optical modulator operating at cryogenic temperatures. *Nat. Mater. 2020 1911*, 19(11):1164–1168, jul 2020.
- [18] Mehrnaz Modaresialam, Zeinab Chehadi, Thomas Bottein, Marco Abbarchi, and David Grosso. Nanoimprint Lithography Processing of Inorganic-Based Materials. *Chemistry of Materials*, 33(14):5464–5482, jul 2021.
- [19] C. J. Xiao, C. Q. Jin, and X. H. Wang. Crystal structure of dense nanocrystalline BaTiO₃ ceramics. *Mater. Chem. Phys.*, 111(2-3):209–212, oct 2008.
- [20] Viola Valentina Vogler-Neuling, Romolo Savo, David Pohl, Nicholas R. Hendricks, Lukas Lang, Maria Timofeeva, Barbara Schneider, Felix Ulrich Richter, Flavia Timpu, Serge Monneret, Fabian Starsich, and Rachel Grange. Solution-Processed Barium Titanate Nonlinear Woodpile Photonic Structures with Large Surface Areas. *physica status solidi (b)*, 257(5):2070024, may 2020.

- [21] Bryce I. Edmondson, Sunah Kwon, Chon H. Lam, J. Elliott Ortmann, Alexander A. Demkov, Moon J. Kim, and John G. Ekerdt. Epitaxial, electro-optically active barium titanate thin films on silicon by chemical solution deposition. *Journal of the American Ceramic Society*, 103(2):1209–1218, feb 2020.
- [22] Fatih Alarслан, Laura Vittadello, Jonas Klein, Qaiser Ali Khan, Christian Kijatkin, Markus Haase, Helmut Schäfer, Mirco Imlau, and Martin Steinhart. Thin Patterned Lithium Niobate Films by Parallel Additive Capillary Stamping of Aqueous Precursor Solutions. *Advanced Engineering Materials*, 24(6):2101159, jun 2022.
- [23] Jiyoung Moon, Masoud Alahbakhshi, Abouzar Gharajeh, Quanwei Li, Zhitong Li, Ross Haroldson, Sunah Kwon, Roberta Hawkins, Moon J. Kim, Walter Hu, Xiang Zhang, Anvar Zakhidov, and Qing Gu. Quasi-CW Lasing from Directly Patterned and Encapsulated Perovskite Cavity at 260 K. *ACS Photonics*, 9(6):1984–1991, jun 2022.
- [24] S. Hirano, S. Shimada, and M. Kuwabara. Fabrication and optical reflection behavior of a two-dimensional barium titanate ceramic photonic crystal. *Applied Physics A 2004* 80:4, 80(4):783–786, feb 2005.
- [25] Hatice Altug, Dirk Englund, and Jelena Vučković. Ultrafast photonic crystal nanocavity laser. *Nat. Phys.* 2006 27, 2(7):484–488, jul 2006.
- [26] Mingxiao Li, Hanxiao Liang, Rui Luo, Yang He, and Qiang Lin. High-Q 2D Lithium Niobate Photonic Crystal Slab Nanoresonators. *Laser & Photonics Reviews*, 13(5):1800228, may 2019.
- [27] Séverine Diziain, Reinhard Geiss, Matthias Zilk, Frank Schrempel, Ernst Bernhard Kley, Andreas Tünnermann, and Thomas Pertsch. Second harmonic generation in free-standing lithium niobate photonic crystal L3 cavity. *Applied Physics Letters*, 103(5):051117, aug 2013.
- [28] T F Krauss. Slow light in photonic crystal waveguides. *J. Phys. D Appl. Phys.*, 40:2666–2670, 2007.
- [29] Guo Jing Tang, Xin Tao He, Fu Long Shi, Jian Wei Liu, Xiao Dong Chen, and Jian Wen Dong. Topological Photonic Crystals: Physics, Designs, and Applications. *Laser Photon. Rev.*, 16(4):2100300, apr 2022.
- [30] Mario Hentschel, Kirill Koshelev, Florian Sterl, Steffen Both, Julian Karst, Lida Shamsafar, Thomas Weiss, Yuri Kivshar, and Harald Giessen. Dielectric Mie voids: confining light in air. *Light: Science & Applications* 2023 12:1, 12(1):1–12, jan 2023.
- [31] Donato Conteduca, Isabel Barth, Giampaolo Pitruzzello, Christopher P. Reardon, Emiliano R. Martins, and Thomas F. Krauss. Dielectric nanohole array metasurface for high-resolution near-field sensing and imaging. *Nature Communications* 2021 12:1, 12(1):1–9, jun 2021.
- [32] Michael R Beaulieu, Nicholas R Hendricks, and James J Watkins. Large-Area Printing of Optical Gratings and 3D Photonic Crystals Using Solution-Processable Nanoparticle/Polymer Composites. 2014.

- [33] Pengfei Qiao, Weijian Yang, and Connie J. Chang-Hasnain. Recent advances in high-contrast metastructures, metasurfaces, and photonic crystals. *Advances in Optics and Photonics*, 10(1):180, January 2018.
- [34] Momchil Minkov, Ian A. D. Williamson, Lucio C. Andreani, Dario Gerace, Beicheng Lou, Alex Y. Song, Tyler W. Hughes, and Shanhui Fan. Inverse design of photonic crystals through automatic differentiation. *ACS Photonics*, 7(7):1729–1741, June 2020.
- [35] Lei Kang, Huaguang Bao, and Douglas H. Werner. Efficient second-harmonic generation in high q-factor asymmetric lithium niobate metasurfaces. *Opt. Lett.*, 46(3):633–636, Feb 2021.
- [36] Gabriel W. Castellanos, Ping Bai, and Jaime Gómez Rivas. Lattice resonances in dielectric metasurfaces. *Journal of Applied Physics*, 125(21):213105, jun 2019.
- [37] Jolanda S. Müller, Andrea Morandi, Rachel Grange, and Romolo Savo. Modeling of Random Quasi-Phase-Matching in Birefringent Disordered Media. *Phys. Rev. Appl.*, 15(6):064070, jun 2021.
- [38] Ruzan Sokhoyan, Prachi Thureja, Jared Sisler, Meir Grajower, Komron Shayegan, Eyal Feigenbaum, Selim Elhadj, and Harry A. Atwater. Electrically tunable conducting oxide metasurfaces for high power applications. *Nanophotonics*, 12(2):239–253, jan 2023.
- [39] Grégoire Saerens, Lukas Lang, Claude Renaut, Flavia Timpu, Viola Vogler-Neuling, Christophe Durand, Maria Tchernycheva, Igor Shtrom, Alexey Bouravleuv, Rachel Grange, and Maria Timofeeva. Image-based autofocusing system for nonlinear optical microscopy with broad spectral tuning. *Opt. Express*, 27(14):19915–19930, Jul 2019.